AGU PUBLICATIONS

JGR

Journal of Geophysical Research: Atmospheres

RESEARCH ARTICLE
10.1002/2017JD026552

Key Points:
- We quantify the fraction of low-level clouds using lidar and the DARDAR satellite data product at the northern edge of the Southern Ocean
- DARDAR underestimates low-level cloud occurrence (0.2-1.0 km altitude) by a factor of 3 compared with surface lidar
- A 5°C difference between lidar and DARDAR T at which half the supercooled clouds glaciate is consistent with NH results.

Correspondence to:
S. P. Alexander,
simon.alexander@aad.gov.au

Citation:
Alexander, S. P., & Protat, A. (2018). Cloud properties observed from the surface and by satellite at the northern edge of the Southern Ocean. *Journal of Geophysical Research: Atmospheres*, *123*, 443–456. https://doi.org/10.1002/2017JD026552

Received 23 JAN 2017
Accepted 29 NOV 2017
Accepted article online 6 DEC 2017
Published online 9 JAN 2018

Cloud Properties Observed From the Surface and by Satellite at the Northern Edge of the Southern Ocean

S. P. Alexander[1,2] **and A. Protat**[3]

[1] Australian Antarctic Division, Hobart, Tasmania, Australia, [2] Antarctic Climate and Ecosystems Co-operative Research Centre, University of Tasmania, Hobart, Tasmania, Australia, [3] Bureau of Meteorology, Melbourne, Victoria, Australia

Abstract A Raman depolarization lidar was deployed at Cape Grim, Australia (40.7°S, 144.7°E), at the northern edge of the Southern Ocean from July 2013 to February 2014 from which we determine cloud boundaries, cloud phase, ice virga, and cloud effective top heights. We compare surface-based lidar with results from the raDAR/liDAR (DARDAR) data set within 1,000 km of Cape Grim. DARDAR combines information from the CloudSat and Cloud-Aerosol Lidar with Orthogonal Polarization (CALIOP) instruments. We extract single-layer clouds that are sufficiently thin for signal to be present on the farside of the cloud and which have a liquid cloud top phase. These conditions maximize the likelihood that both surface-based lidar and DARDAR are observing the full vertical extent of the same clouds. Differences in low-level cloud occurrence frequencies for these single-layer clouds reveal that DARDAR underestimates cloud at 0.2–1.0 km altitude by a factor of 3 compared with the surface-based lidar. When multiple cloud decks are present, the underestimate in this altitude region is around 2.5 times. Heterogeneous glaciation observed by the Cape Grim lidar in midlevel stratiform supercooled water clouds is similar to that reported by previous surface-based observations adjacent to the Southern Ocean, with half of these clouds precipitating ice at cloud top temperatures of −20°C. This transition occurs around −15°C in the DARDAR data set, and this difference is likely due to the reduced sensitivity of surface-based lidar in detecting precipitating ice compared with what a surface-based radar could observe.

1. Introduction

The Southern Ocean is one of the cloudiest places on earth, as a result of the continuous passage of extratropical cyclones and their associated frontal cloud systems (Stubenrauch et al., 2013). Low clouds are particularly dominant over the Southern Ocean when compared with other regions. Yet clouds over the Southern Ocean remain poorly understood and thus poorly represented in reanalyses and coupled climate models (Bodas-Salcedo et al., 2016; Fletcher et al., 2016; Grise et al., 2015; Haynes et al., 2011; McCoy et al., 2016; Naud et al., 2014; Trenberth & Fasullo, 2010). Model simulations indicate large Southern Ocean cloud and radiation biases compared with observations: too much shortwave radiation is absorbed in this region, which induces warm sea surface temperature biases (Grise et al., 2015; Trenberth & Fasullo, 2010). This radiative bias interacts with the location of the tropopause jet in climate models (Ceppi et al., 2012, 2014). Model simulations and reanalyses suggest that a major contributor to this bias is a lack of clouds in the cold sectors of cyclones (Bodas-Salcedo et al., 2014). The few climate models that have the correct zonal mean reflected shortwave radiation in the Southen Ocean region do so through compensating errors. In the warm sectors of the cyclones, these models have high clouds that are too reflective (Bodas-Salcedo et al., 2014).

Satellite retrievals over the Southern Ocean indicate a higher frequency of occurrence of multilayer mixed-phase clouds than at similar northern latitudes (Ceppi, Hartmann, & Webb, 2016; Ceppi, McCoy, & Hartmann, 2016; Choi et al., 2014; Huang et al., 2014; Komurcu et al., 2014; Marchand et al., 2009; McCoy et al., 2014, 2015, 2016; Morrison et al., 2011; Storelvmo et al., 2015; Tan et al., 2016; Tan & Storelvmo, 2016; Tsushima et al., 2006). The higher occurrence of these clouds, which contain supercooled liquid water (SLW) droplets, may play a role in the overall shortwave radiation bias present in climate models (Atkinson et al., 2013; Murray et al., 2012). At temperatures between −40°C and 0°C, heterogeneous freezing takes place to form ice clouds. Ice formation occurs on aerosol particles which act as cloud condensation or ice nuclei. The proportion of clouds which glaciate at a given temperature is partially a function of aerosol loading and varies depending upon location.

A higher proportion of supercooled liquid water clouds exist at lower temperatures in environments that are less polluted (Atkinson et al., 2013; Hu et al., 2010; Kanitz et al., 2011; Murray et al., 2012; Tan et al., 2014; Wilson et al., 2015).

The CALIOP (Cloud-Aerosol Lidar with Orthogonal Polarization) instrument on board the CALIPSO (Cloud-Aerosol Lidar and Infrared Pathfinder Satellite Observations) satellite (Winker et al., 2007) provides vertical profiles of lidar backscatter and depolarization. CALIOP collects data at 1,064 nm and at 532 nm, at which wavelengths it is sensitive to backscatter by spherical liquid droplets and ice crystals. CALIOP separates cloud phase according to different relationships between layer-integrated backscatter and depolarization at 532 nm (Hu et al., 2009). Lidar can easily detect optically thin clouds (those with optical depths less than around 3), but it is incapable of penetrating thick clouds as the lidar signal is rapidly attenuated. CloudSat flies in the same satellite constellation as CALIPSO (the A-Train) and has a cloud-profiling radar (CPR) operating at 94 GHz (Stephens et al., 2002). The CPR has lower sensitivity than CALIOP for optically thin liquid and ice clouds and has difficulty resolving boundary layer clouds due to ground clutter. On the other hand, the radar signal can penetrate optically thick clouds. CloudSat has operated in daylight-only mode since 2011.

To combine the strengths of the CALIOP and CloudSat satellite data products to obtain a more complete cloud climatology, Delanöe and Hogan (2010) developed the raDAR/liDAR (DARDAR) algorithm. DARDAR provides vertically resolved profiles of cloud phase, including supercooled liquid water and mixed-phase clouds. The DARDAR algorithm determines cloud ice properties and identifies supercooled liquid water clouds by using the strong backscatter from the CALIOP lidar signal, and ERA-Interim reanalysis temperatures. Mixed-phase clouds are identified by DARDAR when both radar and lidar return signals are apparent (Delanöe & Hogan, 2010). DARDAR classifies regions as "unknown" when the lidar signal is extinguished but there is likely cloud present in the radar data. As such, DARDAR, and indeed any combined radar-lidar satellite product using CALIOP and CloudSat, underestimates cloud occurrence below 1.5 km altitude (Protat et al., 2014). Given the ubiquity of low-level clouds over the Southern Ocean (Haynes et al., 2011, 2012), this would be a considerable limitation on the usefulness of the DARDAR data set in the boundary layer in this region of the world.

Surface-based lidar observations indicate the prevalence of liquid clouds adjacent to the Southern Ocean at temperatures lower than −25°C (Kanitz et al., 2011). While the combination of satellite radar and lidar permits a more accurate quantification of cloud phase throughout the atmosphere, there remains a high degree of uncertainty of this phase below cloud top height and in the presence of multiple cloud decks (Mace, 2010). Thus surface-based observations are required to provide information on cloud thermodynamics in the lower troposphere, which is especially necessary in the data-sparse Southern Ocean region. Surface-based radars can readily detect large ice particles that appear in low numbers but have difficulty detecting liquid droplets that are small but numerous (Protat et al., 2006, 2010). Conversely, surface-based lidars easily detect liquid water layers, which appear strongly in lidar backscatter profiles (Illingworth et al., 2007). However, the lidar signal is severely attenuated by the liquid cloud layers (Delanöe & Hogan, 2010). Thus, the combination of surface-based radar and lidar is particularly useful in validating satellite retrievals (Protat et al., 2010). Nonetheless, a surface-based lidar alone still provides valuable evaluations of satellite retrievals as we will demonstrate below.

Validation of satellite cloud products is particularly important in the Southern Ocean given the ubiquity of low-level clouds and the paucity of surface data (Haynes et al., 2011; Marchand et al., 2010; McCoy et al., 2014). Indeed, few in situ or surface-based observations of clouds have occurred above or in the vicinity of the Southern Ocean. Two in situ research flights over the Southern Ocean found relatively large amounts of supercooled liquid water and little ice at temperatures down to −22°C (Chubb et al., 2013). Recent case studies of post-frontal clouds near Tasmania incorporated surface-based lidar data from Hobart (43°S) with in situ aircraft flights and CALIPSO satellite data to evaluate the performance of a forecast model (Huang et al., 2015). Lidar observations of clouds during short campaigns (duration of a few months at most) have been performed on board a ship and at the bottom of South America and South Africa (Kanitz et al., 2011). Nonetheless, a quantification of cloud parameters and satellite validation remains elusive in the Southern Ocean. The objective of this paper is to begin to fill these gaps in our knowledge by investigating the structure, phase, and occurrence frequency of clouds observed by a surface-based lidar at Cape Grim (40.7°S, 144.7°E), which is located at the northern edge of the Southern Ocean.

The paper is organized as follows. In section 2, we present a description of the Cape Grim lidar instrument and describe the details of the cloud boundary detection algorithm. Cloud phase detection is also described in this section, along with the conditions required for identifying virga. We describe our use of the DARDAR data

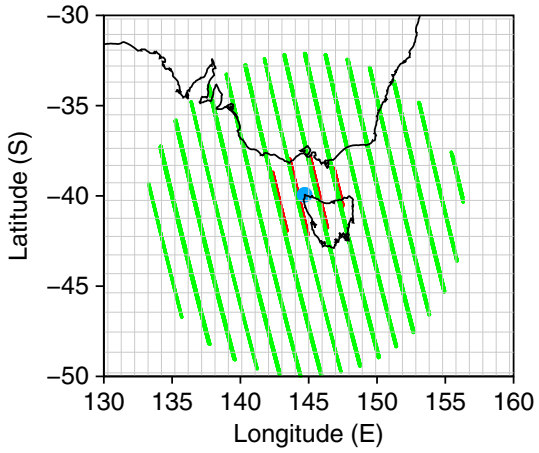

Figure 1. The location of Cape Grim (light blue circle) along with the locations of the DARDAR overpass tracks within 1,000 km of Cape Grim (green) and within 250 km of Cape Grim (red, offset 0.5° eastward for clarity) during August 2013. The 1°×1° gridded ERA-Interim data used in this analysis are also indicated.

set for this analysis in section 2.3. Results are presented in section 3, where a case study of a cold front over Cape Grim is first used to illustrate the cloud detection algorithm before a statistical cloud overview is presented. Later in section 3, we quantify the underestimation of low-level cloud occurrence by DARDAR, before investigating mixed-phase partitioning in midlevel stratiform supercooled liquid water clouds. A discussion section then precedes our conclusions.

2. Data Analysis

2.1. Raman Lidar

A Leosphere R-MAN510 Raman UV polarization lidar was located at Cape Grim between May 2013 and May 2014. The location of Cape Grim is marked in Figure 1 along with the locations of the DARDAR curtains during August 2013. The lidar operates at 355 nm and returns the vertically resolved elastic backscatter signal $P(r)$, where r is altitude, in the parallel and perpendicular directions. The lidar also has a Raman channel at 387 nm, although the Raman data are not required for this analysis. Horizontally oriented plate ice crystals produce nondepolarizing specular reflections, which lead to ambiguity in assigning cloud phase in a vertically pointing lidar system. To avoid this effect, the lidar is tilted at 4° off zenith, which ensures unambiguous cloud phase identification. Data collected from July 2013 until February 2014 inclusive are analyzed due to the higher data availability between these months. The fraction of time each month at which the lidar is operational is illustrated in Figure 2, where it is apparent that only 2 months had lidar data collection exceeding 80%. The total number of days on which any lidar data were collected during this period is 141.

The vertical resolution of the lidar is 15 m, and the temporal resolution is 1 min. To increase the signal-to-noise ratio of thin cloud layers, we temporally average the data for 5 min. We retain the original vertical resolution of 15 m in the data processing because of the desire to determine accurately the altitudes of the cloud bases and cloud tops. ERA-Interim reanalysis data (Dee et al., 2011) provide the background temperature data for the Cape Grim lidar analysis. The 6-hourly reanalysis data are interpolated to the same temporal and vertical grid spacing as the lidar data set, and the four closest reanalysis points around Cape Grim are then averaged to produce one temperature data set.

The range-corrected returned backscatter signal profiles $r^2P(r)$ provided by the lidar are uncalibrated and so require correction for laser output energy and other instrument-specific variables. The calibration is performed by normalizing the value of $r^2P(r)$ observed during cloud-free nighttime intervals between 2.5 and 5.5 km to that expected by molecular scattering alone. We define a cloud-free night as one during which no clouds are detected by our algorithm. This layer is above the boundary layer where aerosol effects would be expected to be largest but low enough to ensure consistently high return signal power. ERA-Interim reanalysis data provide the background atmospheric parameters needed to determine the molecular scattering. The background signal return count of the lidar system decreases over the July to February period. For a given day, the calibration factor is the mean determined over a 5 day interval (±2 days). If five consecutive days are cloudy at altitudes below 5.5 km, or the lidar does not operate during nighttime, a three-point smoothed monthly mean background is used instead.

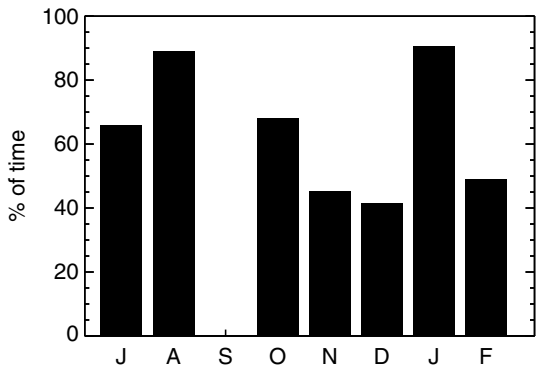

Figure 2. The fraction of time each month for which the lidar is operational.

There is incomplete overlap between the Cape Grim lidar's transmission beam and the field of view of the receiver below 0.5 km altitude as the two are not coaxial. This manifests itself as a consistently increasing backscatter signal with altitude from the surface up to ~0.5 km altitude, as an increasingly larger fraction of backscattered laser light is incident upon the telescope. The cloud detection algorithm detailed below finds cloud bases where the backscattered lidar signal increases with altitude. Thus, without correction for this incomplete overlap, cloud base detection is not possible below about 0.5 km. In order to decrease the minimum altitude at which cloud bases may be detected, we experimentally characterize an overlap function using cloud-free profiles.

This overlap function is used to correct the return signal at altitudes below 0.5 km so that the background (cloud-free) backscattered signal decreases with increasing altitude.

2.2. Cloud Boundaries and Phase Classification

2.2.1. Detection of Cloud Boundaries

The cloud boundary detection algorithm of Wang and Sassen (2001) is applied to the Cape Grim lidar data, with some modifications as detailed below. Requiring the backscatter signal from three consecutive altitudes, each with a larger return signal than in the altitude below, is a necessary precondition for identifying a possible cloud base height (Wang & Sassen, 2001). However, we find for our lidar that two consecutive altitudes with increasing backscatter for clouds with base $T < 0°C$ provide a better initial detection. The spurious signals introduced at this stage by this lower threshold (i.e., two altitudes instead of three) are removed by later speckle removal algorithms. The small vertical-scale gradients within a single backscatter profile are determined by linearly fitting the backscatter profile over 200 m altitude, stepping up in altitude by 15 m (Wang & Sassen, 2001). A possible cloud base must meet two further conditions: (i) the backscattered signal exceeds one standard deviation of the gradient; and (ii) the backscattered signal exceeds the noise level, which is determined from a cloud-free nighttime reference.

The detection of cloud top height by lidar is complicated by the attenuation of the laser signal within the cloud. Indeed, lidars cannot resolve cloud top height where cloud optical depths exceed about three. We determine the gradient in $r^2P(r)$ using the three altitudes immediately beneath the cloud base (i.e., the background clear-sky gradient signal) and then determine the minimum height above cloud base at which $r^2P(r)$ falls beneath this clear-sky gradient. A cloud top height is classified as effective if the gradient of $r^2P(r)$ above the cloud top height is 0 and strong signal attenuation (defined as either a minimum in-cloud gradient of < -7 m^{-1} sr^{-1} km^{-1} or an above-cloud gradient of 0; Wang & Sassen, 2001) occurs within the cloud. Otherwise, the cloud top height is classified as actual. The Cape Grim lidar results indicate that 30–40% of all clouds fully attenuate the laser signal.

Multiple cloud decks can be resolved by this algorithm, assuming that sufficient lidar signal penetrates the lower level cloud(s). This cloud detection algorithm is based on gradients of the backscattered signal, not its calibrated value; thus, detection of weak upper-layer clouds is still achievable provided sufficient signal is returned. We extend the Wang and Sassen (2001) algorithm into our cross-polarization channel. While faint ice clouds do not produce sufficient backscatter to pass the detectability criteria in the copolarization channel, their strong depolarization results in a detectable signal in the cross-polarization channel. The same cloud base and cloud top detection algorithm is run for the cross-polarization channel. Ice clouds in the cross-polarization channel are retained and used in the production of the final merged cloud data product.

During periods of fog, drizzle, or rain, or where there is very low cloud base (apparent from a visual inspection of the data), the algorithm cannot determine a cloud base height due to weak or nonexistent vertical gradients in return signal power beneath the base. Visual inspection of the data reveal that cloud base heights below about 50 m, especially during periods of rain or drizzle, are ill defined. These ill-defined periods occur in less than 5% of the profiles in which clouds are identified. As these are the lowest-level clouds, we can apply a threshold to determine where the lidar's backscatter values are above the background molecular scattering: the highest altitude where this is true is the effective cloud top height (it is always an effective top because of the complete attenuation of the lidar signal by these clouds). The cloud base height is nominally assigned a value equal to the lowest nonzero altitude (i.e., 15 m).

2.2.2. Cloud Phase Determination and Virga Detection

Lidar-based cloud classification schemes can use simple depolarization δ thresholds; for example, $\delta > 0.11$ defined ice clouds (Intrieri et al., 2002) or discrete δ thresholds based upon a range of lidar backscatter β (Shupe, 2007). We follow the method of Hu et al. (2009) here, where the boundary between ice and water is a linear function of layer-integrated calibrated backscatter β and layer δ. Integration of the β and δ over the cloud layer also reduces noise inherently associated with determining cloud phase using individual pixels. The presence of horizontally oriented plate-like ice crystals in the liquid water subset is negligible given the off-zenith lidar tilting.

An additional constraint is imposed upon the cloud phase, such that all clouds where the ERA-Interim reanalysis temperatures are $> 0°C$ are classified as liquid and all clouds where temperatures are $< -40°C$ are classified as ice. To remove isolated speckled points in the data set, a coherence filter is applied to the cloud phase. We use a 5×5 grid of pixels and set the central pixel to clear if more than 15 pixels themselves are clear, in a similar

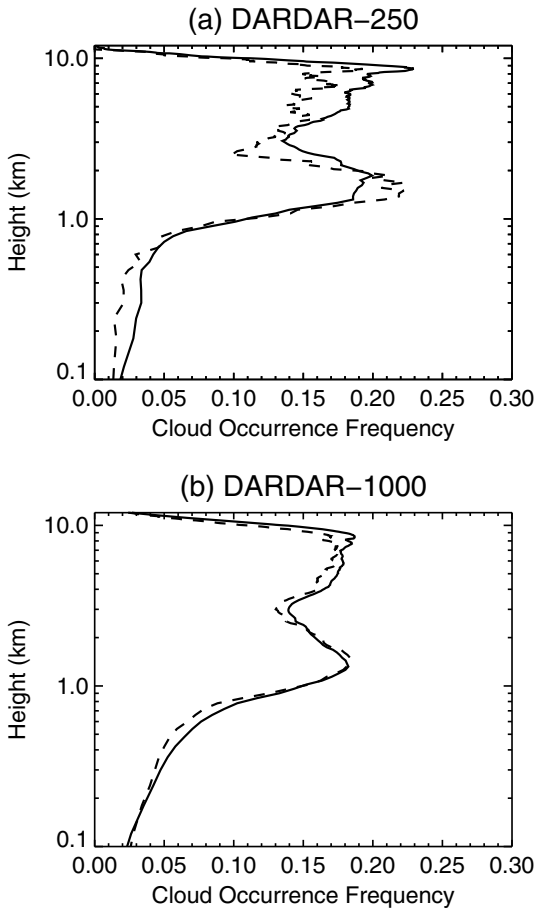

Figure 3. The cloud occurrence frequency calculated using all data (solid lines) and only data within 1 day of surface-based lidar observations (dashed lines) for (a) DARDAR-250 and (b) DARDAR-1000.

approach to Shupe (2007). If the central pixel is not clear, unless there are more than 5 pixels of the same phase as the central pixel, the central pixel is set to the most plentiful cloud phase within the grid. Different sized grids were tested, but this 5×5 grid size was found to be the optimal balance between retaining cloud pixels at the edge of clouds and rejecting most noise.

Ice virga are classified separately from their overlying supercooled liquid water cloud layer. The boundary between the top of the virga and the base of the overlying cloud is readily determined based on different gradients in lidar return signal power (Wang & Sassen, 2001). These ice virga are observed beneath some supercooled liquid layers. Precipitating supercooled liquid water clouds present directly above ice virga can be classified as "mixed-phase" clouds, although these mixed-phase clouds are included in the supercooled water category for this analysis.

Midlevel stratiform altocumulus clouds are readily identified in lidar backscatter return profiles by their strong backscatter in the copolarization channel and low depolarization ratio. These clouds usually persist for tens of minutes to a few hours and generally do not change in altitude by more than a few hundred meters or so during their observation by lidar (Ansmann et al., 2009). Heterogeneous ice formation in these supercooled liquid clouds does not commonly commence until cloud top temperatures fall below −10°C to −20°C (Ansmann et al., 2009; Kanitz et al., 2011; Seifert et al., 2010). The presence of aerosols and dust result in a higher proportion of these midlevel clouds precipitating ice virga for a given temperature than in cleaner conditions (Kanitz et al., 2011). The ice virga detected by our cloud algorithm are used to investigate the proportion of these supercooled liquid clouds which precipitate ice virga at various cloud top temperatures above Cape Grim.

2.3. DARDAR

DARDAR data are gridded at 60 m in the vertical and 1 km in the horizontal. DARDAR v2.2.1 data are used in this analysis (Ceccaldi et al., 2013). Figure 1 showed the location of the CALIOP and CloudSat curtains relative to Cape Grim. It is clear that the satellites do not pass directly overhead of the lidar. To make the closest comparison with the surface data, we spatially average DARDAR. At a typical midtropospheric wind speed of 20 m s^{-1}, a contiguous cloud layer observed by the Cape Grim lidar for 15 min (i.e., three temporal bins) will have a horizontal extent of 18 km; thus, we average the DARDAR into 18 km along-track bins. Altering the horizontal averaging distance has little effect on the results presented below.

Three different subsets of DARDAR are used to compare cloud properties in different spatial regions with those obtained by the Cape Grim lidar: (i) data within 250 km of the Cape Grim lidar, referred to as DARDAR-250; (ii) data within 1,000 km of Cape Grim, referred to as DARDAR-1000; and (iii) Southern Ocean data (40°S–65°S and 100°E–160°E, the same region defined by Huang et al., 2012), referred to as DARDAR-SO. Most of the comparisons between the surface lidar and DARDAR are performed using the DARDAR-1000 subset. Results from the DARDAR-250 region are similar to the DARDAR-1000 results presented below, except that the smaller spatial region has somewhat noisier profiles due to the lower amount of data. There are 184 separate DARDAR-1000 curtains and 44 separate DARDAR-250 curtains during the time period analyzed.

Significant temporal data gaps exist in the Cape Grim lidar record (see Figure 2). The DARDAR-1000 data set is further screened to retain only data within 1 day of data collected by the surface-based lidar. This time period allows ample time for the propagation of synoptic-scale meteorological features through the domain of the satellite data set. Varying this for similar time thresholds has little effect on the results. We demonstrate in Figure 3 the small difference in cloud occurrence frequency at each altitude for both DARDAR-250 and DARDAR-1000 when subsampling the original DARDAR data sets within 1 day of surface-based lidar data collection. This difference is minimal for the DARDAR-1000 data set but somewhat larger in the midtroposphere for DARDAR-250. The cloud occurrence fraction is determined as the ratio of the number of times cloud is present at each altitude to the number of times that altitude is sampled.

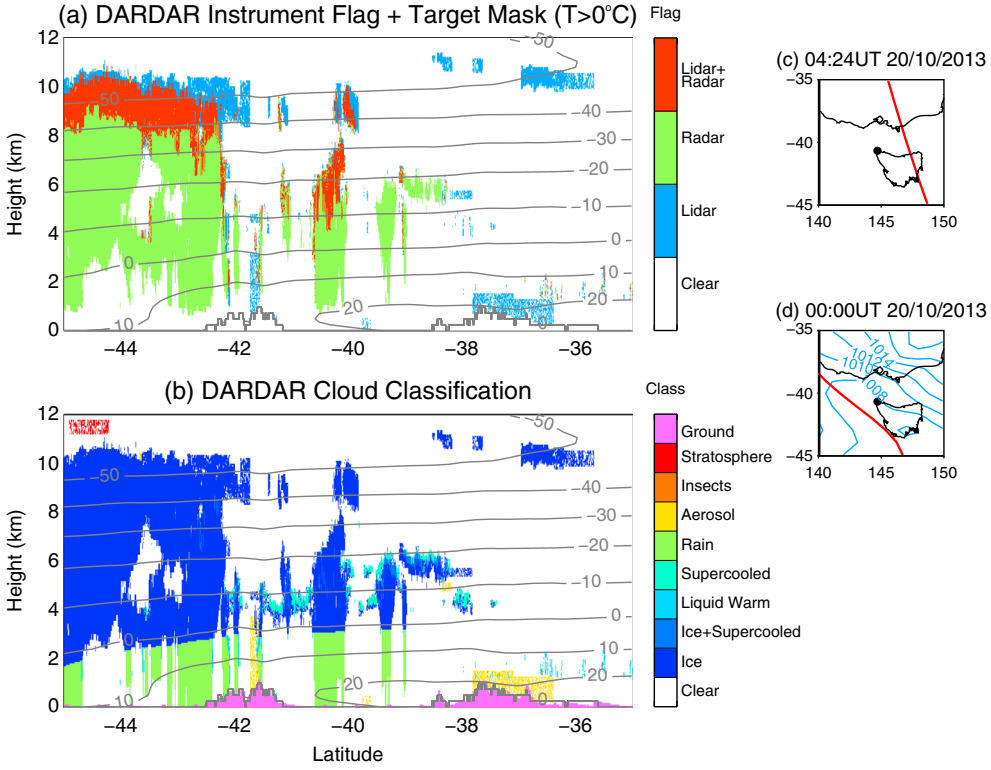

Figure 4. DARDAR results from the overpass of Tasmania at 0424 UT, 20 October 2013: (a) DARDAR instrument flag (for temperatures below 0°C) and target mask (for temperatures above 0°C); (b) DARDAR cloud classification. Temperatures from ERA-Interim are also marked (units of °C). (c) The path of the CALIOP and CloudSat satellites are indicated (red line), along with Cape Grim (black circle). (d) ERA-Interim surface pressure at 0000 UT on 20 October (blue lines, units of hPa) along with the location of the cold front (red line).

3. Results

We present an example of the evolution of the cloud structure and phase during the passage of a cold front, using data from the Cape Grim lidar, along with a curtain of DARDAR results close to Cape Grim. Following this, we discuss statistical cloud properties of the data sets before focussing on an analysis of low-level clouds and in particular the satellite/surface-based lidar differences. Lastly, we examine mixed-phase partitioning of midlevel supercooled liquid water clouds.

3.1. Cloud Structure and Phase During the Passage of a Cold Front

A cold front passed over Cape Grim on 20 October 2013. The sea level pressure, together with the position of the cold front, are shown for 0000 UT on 20 October 2013 in Figure 4d. The 10 m horizontal wind field from ERA-Interim is used to calculate the location of the cold front. Following Simmonds et al. (2012), a possible frontal boundary is defined at locations where the 10 m winds change from the northwest to the southwest quadrant between 6-hourly time steps and the magnitude of the meridional velocity change exceeds 2 m s^{-1}. We apply a cluster analysis to remove isolated points tentatively identified as fronts and retain the easternmost points of each frontal object, before performing repeated smoothing filters on the resultant longitude time series. The frontal points that pass these conditions are then defined as the front at time step $t + 6$ h, which is in closer correspondence to other synoptic fields at this time step than at time t (Papritz et al., 2014). Note that the algorithm to determine the location of the cold front is independent of sea level pressure, yet good agreement between the location and the trough of low pressure is evident in Figure 4d.

The DARDAR instrument flag, target mask, and cloud classification scheme for an overpass of the satellites containing the CALIOP and CloudSat instruments are shown in Figures 4a and 4b, respectively, at 0424 UT on 20 October 2013. We combine the separate DARDAR "instrument flag" and "target mask" data products here because the instrument flag product is related to ice retrieval only, at temperatures below 0°C. The satellites' tracks are indicated in Figure 4c. DARDAR identifies thick ice clouds as low as 2 km altitude and cloud tops

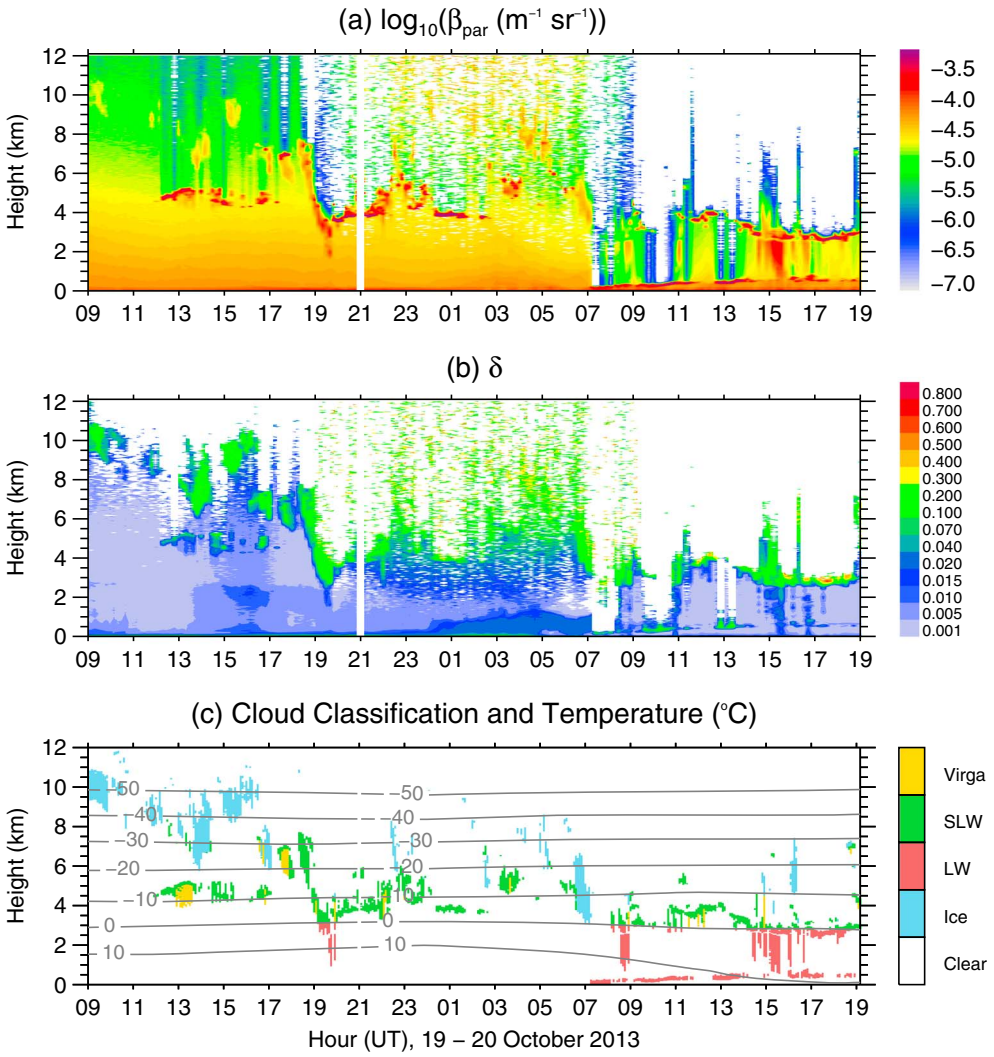

Figure 5. Cape Grim lidar results and output of the cloud detection algorithm from 19 to 20 October 2013. (a) The calibrated coplanar backscatter signal β_{par} (logarithmic scale, units of m^{-1} sr^{-1}); (b) cloud depolarization ratio δ; (c) cloud classification and temperature interpolated from the ERA-Interim reanalysis (lines, units of °C).

at about 10 km. Note that both CALIOP lidar and CloudSat radar data are required to obtain the full depth of the clouds.

The passage of a cold front is characterized by a lowering of the cloud base with time, as is apparent in Figure 5 from the Cape Grim lidar results. High ice clouds (cirrus) above about 7 km altitude are present during the first few hours of this case, as well as midlevel water clouds with ice virga at 4.5 km. Midlevel clouds remain visible throughout the remainder of this frontal passage. Low-level (< 500 m altitude) water clouds occur from 0700 UT on 20 October onward. Multiple cloud decks are readily detected by the algorithm if there is sufficient high-altitude signal (e.g., 1700 UT on 19 October), but thick, low-level clouds fully attenuate the lidar backscattered signal at various times from 0700 UT on 20 October. The higher noise level is clearly evident in the upper troposphere during local daytime (from ~1900 UT on 19 October), which restricts the recoverable cirrus cloud information at this time.

3.2. Statistical Cloud Properties

The monthly cloud fraction calculated from DARDAR and the surface lidar are shown in Figure 6 for July 2013 to February 2014 along with the International Satellite Cloud Climatology Project (ISCCP) climatology (Rossow & Schiffer, 1999; Schiffer & Rossow, 1983). These monthly fractions for surface and satellite results are the ratio of the number of cloud observations at any altitude to the total number of observations made each month, excluding rainfall and aerosol. Cloud coverage fraction calculated from the Cape Grim lidar data are lower

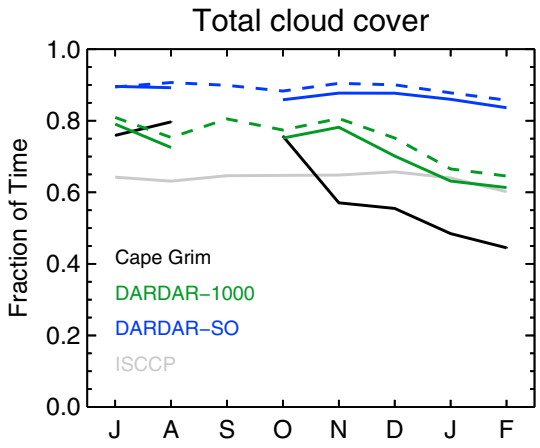

Figure 6. Monthly cloud fraction reported by the Cape Grim lidar (black), DARDAR-1000 (green), and DARDAR-SO (blue). The solid DARDAR lines indicate data that are subset to be within 1 day of a surface-based observation, while the dashed DARDAR lines indicate cloud fraction using all data. The ISCCP climatology from the grid point closest to Cape Grim is also marked (gray).

than that calculated from the DARDAR-1000 data set. It is possible that some of this deficiency in total cloud cover reported by the surface-based lidar is due to its difficulty in resolving cirrus clouds during daytime. The monthly cloud cover is about 5% larger for both DARDAR-1000 and DARDAR-SO regions, when considering the full data sets (dashed lines in Figure 6).

The occurrence distribution frequencies of cloud base height and cloud top height for the Cape Grim lidar along with DARDAR-1000 and DARDAR-SO are shown in Figure 7. Each cloud layer at times of multiple cloud decks is treated as a separate event in the data sets. The Cape Grim occurrence distributions are for clouds where backscatter signal is present above the cloud and thus do not include thick cloud, near-surface cloud, or fog. Similarly, the occurrence distributions for the DARDAR data are for profiles without the unknown classification beneath a cloud base. The cumulative distribution frequencies shown here in Figure 7, and in subsequent plots, are normalized. The actual number of data points used to form these distributions is different for each of the lidar and satellite data sets. The DARDAR regions indicate more bases and tops at higher altitudes than Cape Grim. The lidar reports about 60% of cloud bases below 1.0 km compared with $<20\%$ for DARDAR. Similarly, the surface-based lidar results indicate that about 35% of cloud tops are below 1.0 km compared with $<10\%$ for both these DARDAR regions.

3.3. Low-Level Cloud Statistics

We examine the distribution of the lowest cloud base from each profile in the surface and DARDAR-1000 data sets in Figure 8. This avoids the limitations due to Cape Grim lidar signal attenuation of higher-level clouds when thick multiple cloud decks are present. The probability distribution of DARDAR is shifted to higher altitudes compared with Cape Grim. The surface-based data indicate that 50% of all cloud base heights occur below 500 m altitude and 70% below 1 km altitude. This contrasts with the 10% for DARDAR-1000 below 500 m altitude and about 30% below 1 km altitude. The steep gradient of the DARDAR curve indicates that a substantial proportion of the satellite-derived lowest cloud base heights are between 1 and 2 km altitude. Including the DARDAR rain class with the DARDAR clouds does not account for the satellite-based underestimate of low-level cloud compared with the surface-based observations.

To investigate further the regions of the troposphere where cloud detection by radar or lidar predominantly occurs around Cape Grim, the cloud base height and cloud top height cumulative probability distributions for the Cape Grim lidar and DARDAR-1000 at times when only a single layer of cloud was detected, and signal is observed on the farside of the cloud, are shown in Figure 9. Figure 9 indicates that the "radar only" (i.e., from CloudSat) has lower cumulative probabilities below 1 km than the "lidar only" (from CALIOP).

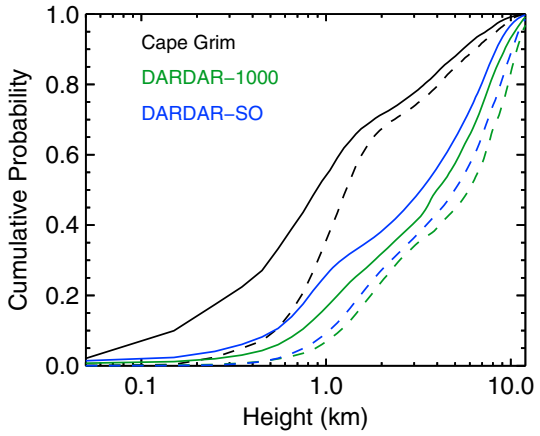

Figure 7. The cumulative probability distributions of cloud base height (solid lines) and cloud top height (dashed lines) for the Cape Grim lidar data (black), DARDAR-1000 (green), and DARDAR-SO (blue) where sufficient signal is present on the farside of the cloud.

The cloud occurrence fractions at each altitude are presented in Figure 10 for multiple clouds and single clouds with liquid tops. The occurrence fraction is the ratio of the number of times cloud is present at each altitude to the number of times that altitude is sampled. For these data, a cloud occurrence fraction of 0.02 corresponds to $\sim$800 events recorded in the Cape Grim data set and $\sim$190 events in the subset DARDAR-1000 data set (i.e., subset to only include data within 1 day of surface observations; however, the distribution is very similar for the full DARDAR-1000 data set—not shown). The satellites pass over regions of mountainous terrain of altitude $<$ 1 km (e.g., to the southeast of Cape Grim, over central Tasmania; see Figure 1). In forming the DARDAR regional cloud occurrence fractions, observations flagged as "ground" in the DARDAR data products are not included in determining the number of times which that particular altitude is sampled. The results shown below do not change if we replace all ground classifications in the DARDAR data set with a "cloud" classification; nor do the results change if the entire vertical profiles above mountainous regions are excluded from the DARDAR-1000 analysis.

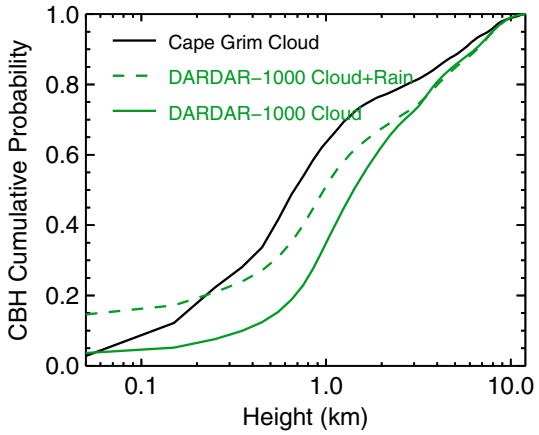

Figure 8. The cumulative probability distributions of the lowest detected cloud base height for each profile for the Cape Grim lidar (black) and DARDAR-1000 (green). The lowest altitude is at 50 m. The DARDAR-1000 cumulative probability also including the "rain" classification is indicated by the dashed green line.

Profiles that have more than one discrete cloud layer are extracted to form Figure 10a. This result is formed from vertical profiles that do not have the unknown on the farside of the cloud for DARDAR nor the "effective" cloud top height for Cape Grim; that is, sufficient signal is present on the farside of the cloud. As such, these cloud fractions will be lower bounds of their actual occurrence as thick clouds are discarded in this analysis. The larger middle- and upper-tropospheric cloud occurrence is clearly apparent in DARDAR-1000.

We extract the subset of clouds that are single layer, sufficiently thin for signal to be present on the farside of the cloud, and that have a liquid cloud top phase. These conditions maximize the likelihood that both surface-based lidar and DARDAR are observing the full vertical extent of the same clouds. The results, presented in Figure 10b, indicate a similar, albeit low, cloud occurrence fraction above ~1.5 km altitude. Below ~1.5 km altitude, a much higher fractional cloud occurrence is reported by the surface-based lidar than DARDAR-1000. Although not shown here, we note that the DARDAR-250 data are similar to Figure 10, albeit with more noise.

3.4. Supercooled Liquid Water Clouds

The supercooled liquid water (SLW) cloud occurrence, represented as the fraction of all observations, is shown in Figure 11. The Cape Grim lidar cloud classification algorithm detailed above incorporates mixed-phase as part of its "SLW" class. The DARDAR-1000 combined "SLW + Mix" classes shows a similar vertical distribution to the Cape Grim results. Peak SLW occurrence is ~1.5 km altitude in the Cape Grim data set and 2 km altitude in the DARDAR-1000 data set. This offset of 0.5 km in the peak SLW occurrence between ground-based lidar and DARDAR is likely attributable to the attenuation of signal through these optically thick clouds and the difficulty of these satellites to observe fully low-level clouds, resulting in an underestimate of SLW. Both DARDAR-1000 and the surface data have a low SLW occurrence fraction in the midtroposphere, decreasing to negligible values above 7–8 km altitude.

Midlevel stratiform clouds are present in the lidar copolarization returns, for example, from 1200 UT on 19 October at 4.5 km in Figure 5. These clouds are less complex than convective clouds for studying heterogeneous ice nucleation and additionally, for at least some of the observation of the cloud, are usually sufficiently transparent to lidar to enable a determination of cloud top height. To investigate mixed-phase partitioning over a range of cloud top temperatures of these midlevel stratiform clouds in the vicinity of Cape Grim, we retain SLW cloud layers that persist for at least 15 min, have an "actual" cloud top height for at least one vertical profile within the cloud, remain at fairly constant altitude during the observation interval (cloud base height changes less than <0.5 km), and have vertical extent of <0.5 km (Ansmann et al., 2009). Cloud tops need to be determined as heterogeneous nucleation typically begins in this coldest part of the cloud (Rauber & Tokay, 1991). The ice virga detected using the method described in section 2 allows separation of an individual cloud layer into precipitating (thus, likely mixed phase) or nonprecipitating (assumed to be pure supercooled liquid water). We assume that the presence of ice virga below a supercooled liquid water cloud is evidence that in-cloud thermodynamic conditions are appropriate for ice formation which increase in size and so precipitate out of the cloud quickly (Ansmann et al., 2009). Thus, a supercooled liquid water (SLW) cloud with ice virga beneath is classified as an "ice-containing cloud" (or "mixed-phase cloud"), while clouds without virga are pure liquid water.

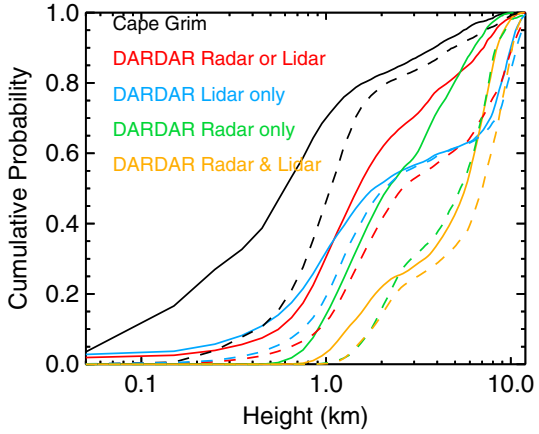

Figure 9. Cloud base (solid lines) and cloud top (dashed lines) height cumulative probabilities for single-layer clouds for Cape Grim where there is signal on the farside of the cloud (black), all DARDAR-1000 data observed by either CloudSat or CALIOP (red), DARDAR-1000 data which CALIOP only observes (blue), DARDAR data which only CloudSat observes (green), and DARDAR-1000 data which both CALIOP and CloudSat observe (yellow).

Figure 12 shows the fraction of these midlevel SLW clouds which precipitate ice as a function of cloud top temperature. Data from field campaigns adjacent to the Southern Ocean presented by Kanitz et al. (2011) are overplotted for reference: although for clarity their uncertainties are not added, we note that these are mostly around ±10%. The uncertainties on the Cape Grim data indicate the standard error $\sigma = \sqrt{f(1-f)/n}$ where n is the number of clouds and f the fraction of ice-precipitating clouds (Seifert et al., 2010).

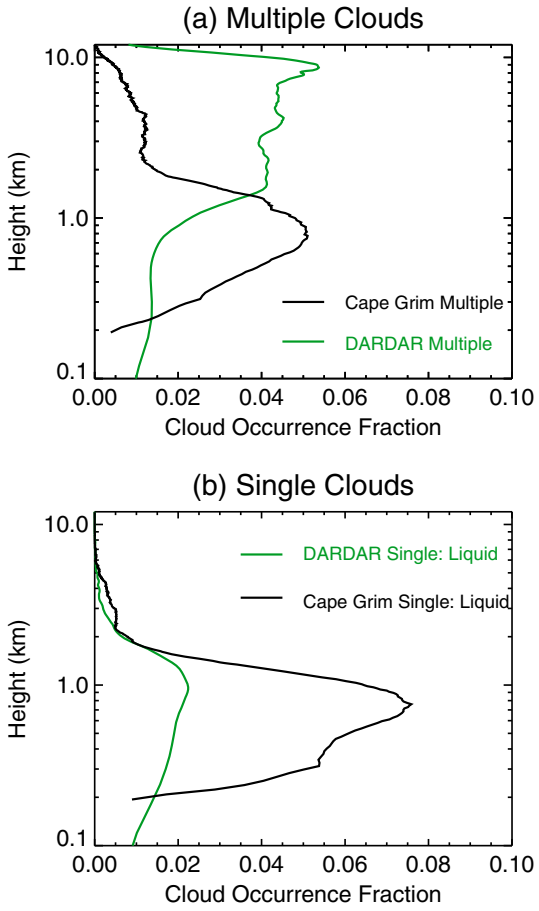

Figure 10. The cloud occurrence fraction at each altitude for Cape Grim (black) and DARDAR-1000 (green). (a) Cloud occurrence fraction for multiple clouds present in vertical profiles. (b) Cloud occurrence fraction for single clouds present in vertical profiles, where the highest cloud top phase is liquid.

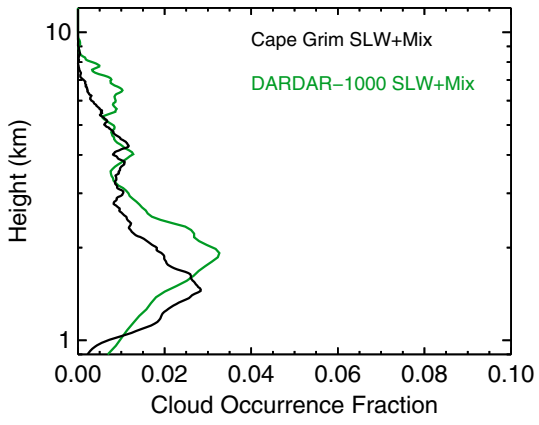

Figure 11. The total supercooled liquid cloud occurrence fraction (which includes mixed-phase clouds) at each altitude for the Cape Grim lidar (black) along with the total "SLW plus Mix" fraction for DARDAR-1000 (green).

The atmosphere above Cape Grim shows heterogeneous ice glaciation in these midlevel supercooled water clouds similar to other midlatitude sites adjacent to the Southern Ocean (Punta Arenas and Stellenbosch), although the Cape Grim data are from a longer-duration campaign. A large increase in the fraction of ice-containing clouds is evident above Cape Grim as the temperature falls below about −20°C. The Cape Grim cloud algorithm may report a cloud effective top height at some or most time steps when observing a SLW cloud; thus, a limitation of this technique is in the assumption that cloud top height of these clouds does not vary enough to move a cloud into an adjacent cloud top temperature bin.

The fraction of glaciating midlevel stratiform supercooled clouds (i.e., clouds that have ice within 0.5 km of the base of the water layer) in the DARDAR-1000 data product that have horizontal extent of at least 18 km is shown in Figure 12. We have assumed that ice directly below a supercooled layer is due to glaciation within the supercooled cloud itself and also note that reducing the horizontal averaging threshold results in a similar distribution to that presented here. The DARDAR-1000 show a similar step in the fraction of glaciating SLW clouds as reported by the Cape Grim lidar. Half of the observed midlevel supercooled clouds are glaciating at −20°C according to the Cape Grim data set, while the DARDAR data set indicates that half are glaciating at a warmer −15°C.

4. Discussion

CloudSat underreports the presence of cloud in the lowest altitudes primarily due to surface radar clutter. CALIOP underreports cloud in these lowest altitudes when its lidar signal is extinguished by higher-level thick cloud. Neither the space-based nor surface-based observations provide the ultimate "truth" of cloud throughout the troposphere. Nonetheless, comparisons between data products derived from observations made with these remote sensing instruments can illuminate the degree by which the lower tropospheric clouds are underestimated by satellite. Blanchard et al. (2014) used surface-based lidar and radar at Eureka, Canada (80°N), to demonstrate a 25% deficit of clouds below 0.5 km altitude (and a 10% deficit at 0.5–1.0 km) compared with surface-based instruments. CloudSat and CALIOP underestimate cloud fraction by about one third around Darwin (12°S) below 1.5 km compared with combined estimates from surface-based lidar and radar (Protat et al., 2014). On the other hand, Mioche et al. (2015) showed an overestimate of low-level cloud fraction by satellite when compared with a surface-based lidar at Ny-Alesund (78°N), although the authors attribute this overestimate to short-duration data set, colocation differences, or different cloud determination algorithms.

While the lack of a cloud radar at Cape Grim precludes a full analysis of the differences between satellite and surface-based instruments throughout the troposphere, we can estimate the deficit using subsets of the data as was presented in Figure 10. DARDAR in the northern part of the Southern Ocean underestimates low-level cloud by a factor of 3. A correction factor is thus recommended to be applied to the DARDAR low-level cloud occurrences in this region to more accurately reflect the true low-altitude cloud occurrences. This factor of 3 is likely to be a lower bound given that the Cape Grim lidar signal cannot penetrate thick cloud; thus, these thick clouds are not included in the analysis. When multiple cloud decks are present, the surface-based lidar also records these low-level clouds about 3 times more often than is present in the satellite data product. This multiple-cloud result is based on a

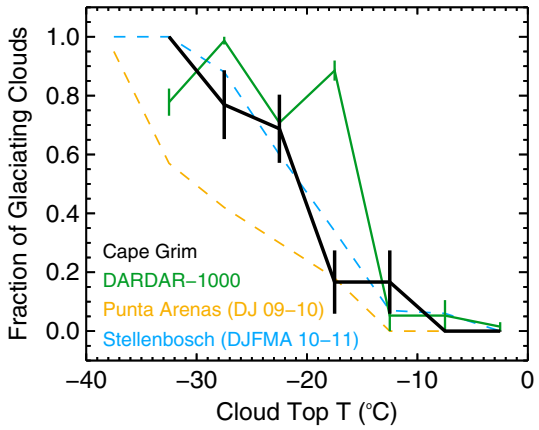

Figure 12. Fraction of midlevel supercooled liquid water clouds below which ice virga are detected, that is, the fraction of clouds which are glaciating, at Cape Grim (black) and for DARDAR-1000 (green) compared with observations made by Kanitz et al. (2011) at Stellenbosch (December 2010 to April 2011, yellow dash) and Punta Arenas (December 2009 to January 2010, blue dash). The standard errors for the Cape Grim and DARDAR data are indicated.

subset of the total number of profiles containing multiple cloud decks as the algorithms require the farside cloud boundary to be defined. Nonetheless, under such circumstances, a similar correction factor to DARDAR could also be applied.

An analysis using the full DARDAR-1000 data set (rather than data within 1 day of Cape Grim lidar observations of Figure 10) indicates that DARDAR underestimates the 0.2–1.0 km altitude clouds by (i) 3.1 times for liquid-topped single-layer clouds and (ii) 2.5 times for profiles with multiple cloud decks. Another source of uncertainty in the results is the fact that the Cape Grim lidar does not collect data continuously (see Figure 2). This could result in incorrect determination of parameters such as the surface-based estimate of cloud fraction, as was found for a reduced data availability study over a midlatitude site in the United States (Kennedy et al., 2014). We perform two types of statistical bootstrapping on the Cape Grim data set to investigate how instrument downtime may affect our results. First, we randomly remove half of the Cape Grim profiles and rerun the analysis, which results in an underestimate of the 0.2–1.0 km single-layer clouds of 3.1 times. Second, we randomly remove half (three quarters) of the days on which lidar measurements were made at Cape Grim and find the underestimate of single-layer clouds to be 3.2 times (2.7 times). The equivalent changes for random removal of half and three quarters of the days on which multiple cloud deck observations were made at Cape Grim are 3.1 and 2.0 times, respectively. Monthly surface-based cloud fraction decreases by up to 10% when either half or three quarters of the days on which Cape Grim lidar profiles were obtained are randomly removed. We conclude, based on these bootstrapping experiments, that the reported DARDAR underestimate of these low-level (0.2–1.0 km altitude) single-layer clouds of about 3 times is robust. We further conclude that the DARDAR underestimate of low-level clouds at times when multiple cloud decks are present is less robust and probably closer to 2.5 times, given the spread of the results obtained under different bootstrapping experiments of ~2–3 times.

In situ aircraft observations over the Southern Ocean reported by Chubb et al. (2013) indicate the prevalence of predominantly liquid low-level clouds with a mix of solid and liquid precipitation. This contrasts with merged satellite data products such as DARDAR, where thin supercooled liquid clouds exist over the Southern Ocean above a glaciating cloud (Huang et al., 2012). The Cape Grim lidar indicates the presence of these thin supercooled liquid clouds above ice virga (see Figure 5) and their increasing likelihood of existence for clouds at colder cloud top temperatures (Figure 12). A similar fraction of clouds above Cape Grim are glaciated when compared with other sites adjacent to the Southern Ocean (Figure 12). Cloud seeding of ice formation by higher-altitude clouds was observed in the tropics from lidar (Ansmann et al., 2009). In the Cape Grim data set, we do not observe evidence of higher-altitude ice acting to seed midlevel supercooled liquid clouds, a result which is in agreement with other midlatitude observations (Seifert et al., 2010). Supercooled liquid layer clouds present in the DARDAR-1000 data set indicate a similar fraction of glaciation to the Cape Grim data, except that the 50% glaciation occurs about 5°C (one cloud top temperature bin) warmer in the satellite data product. Differences between the fraction of glaciated clouds reported by surface-based instruments (using both radar and lidar) and by CALIPSO and CloudSat (not the DARDAR data set) were examined by Bühl et al. (2013). The 50% glaciating threshold is about 5°C higher in the satellite data than in the surface-based lidar data collected in Germany, which is the same as present in the Cape Grim data (Figure 12). The value of additionally having a surface-based radar to measure precipitating ice, some of which is likely undetectable by lidar, results in a shift in the distribution of glaciating clouds to higher temperatures. Thus, the higher sensitivity of a surface-based radar to detect ice crystals can be used to reconcile surface-based and space-based differences (Bühl et al., 2013).

5. Conclusions

Using data collected by a depolarization lidar located at Cape Grim (41°S) between July 2013 and February 2014, we construct a climatology of cloud parameters and compare with the DARDAR v2.2.1 satellite data products obtained within 1,000 km of Cape Grim (referred to as the DARDAR-1000 data set). The parallel and

perpendicular backscattering signals from the Cape Grim lidar are used to determine cloud boundaries, cloud effective tops, cloud phase, and ice virga as described by the algorithm above.

The Cape Grim lidar indicates that for the lowest-level clouds in each profile, 70% of cloud base heights are below 1 km altitude. This contrasts with the lowest-level clouds in each vertical profile reported by DARDAR-1000, which have 20% of cloud base heights below 1 km altitude. By extracting vertical profiles of cloud which are single layer, sufficiently thin for signal to be present on the farside of the cloud, and which have a liquid cloud top phase, we maximize the likelihood that both surface-based lidar and DARDAR are observing the full vertical extent of the same clouds. These conditions allow us to compare the cloud occurrence frequencies reported by satellite and surface-based lidar. For these conditions, the cloud occurrence fraction is 3 times greater in the 0.2–1.0 km altitude range for the Cape Grim lidar than that reported by DARDAR. Thus, a correction factor of about 3 should be applied to the DARDAR cloud occurrence frequencies in this northern region of the Southern Ocean when single-layer liquid cloud tops are present. For multiple cloud decks, a correction factor of about 2.5 can be applied, although this value has a higher uncertainty. The issue of being not able to resolve many low-level clouds is more critical over the Southern Ocean than most other locations worldwide given the preponderance of low-altitude cloud in this region.

Heterogeneous cloud glaciation in thin supercooled liquid water clouds above Cape Grim is similar to that reported during summer campaigns at two other Southern Hemisphere sites abutting the Southern Ocean. The fraction of glaciating clouds reaches 50% as cloud top temperatures fall to −20°C. The DARDAR results show that this transition to predominantly glaciating clouds occurs around −15°C. This discrepancy of 5°C is consistent with results from the Northern Hemisphere and represents a limitation of only having a surface-based lidar to observe precipitating midlevel stratiform clouds.

Comparisons with the DARDAR satellite data products in the vicinity of Cape Grim quantify the fraction by which DARDAR underestimates low-level clouds at the northern edge of the Southern Ocean. While the liquid-ice partitioning of midlevel stratiform supercooled liquid water clouds is similar, albeit shifted to colder temperatures, between lidar and DARDAR, a surface-based cloud radar would likely allow reconciliation between satellite and surface observations of these clouds in the Southern Ocean region. Indeed, the inclusion of a surface-based cloud radar and a microwave radiometer in future studies of Southern Ocean clouds across a range of latitudes would permit satellite retrieval evaluation throughout the troposphere and a full quantification of cloud fraction and phase of the ubiquitous low-level clouds as well as higher-level clouds.

Acknowledgments
ERA-Interim data were downloaded from the ECMWF server, and the DARDAR satellite data products were downloaded from the iCARE (Cloud-Aerosol-Water-Radiation Interactions) server following registration. The Cape Grim lidar data are available from ftp://ftp.bom.gov.au/anon/home/cawcr/perm/CapeGrimLidar.zip. We thank Julien Delanöe for his valuable advice, insights, and comments on the DARDAR data products. We also thank the three anonymous reviewers whose valuable comments on earlier versions of this manuscript improved this study. This research was conducted for project 4292 of the Australian Antarctic program.

References

Ansmann, A., Tesche, M., Seifert, P., Althausen, D., Engelmann, R., Fruntke, J., … Muller, D. (2009). Evolution of the ice phase in tropical altocumulus: SAMUM lidar observations over Cape Verde. *Journal of Geophysical Research*, *114*, D17208. https://doi.org/10.1029/2008JD011659

Atkinson, J. D., Murray, B. J., Woodhouse, M. T., Whale, T. F., Baustian, K. J., Carslaw, K. S., … Malkin, T. L. (2013). The importance of feldspar for ice nucleation by mineral dust in mixed-phase clouds. *Nature*, *498*, 355–358. https://doi.org/10.1038/nature12278

Blanchard, Y., Pelon, J., Eloranta, E. W., Moran, K. P., Delanoë, J., & Seze, G. (2014). A synergistic analysis of cloud cover and vertical distribution from A-Train and ground-based sensors over the high Arctic station Eureka from 2006 to 2010. *Journal of Applied Meteorology and Climatology*, *53*, 2553–2570. https://doi.org/10.1175/JAMC-D-14-0021.1

Bodas-Salcedo, A., Andrews, T., Karmalkar, A. V., & Ringer, M. A. (2016). Cloud liquid water path and radiative feedbacks over the Southern Ocean. *Geophysical Research Letters*, *43*, 10,938–10,946. https://doi.org/10.1002/2016GL070770

Bodas-Salcedo, A., Williams, K. D., Ringer, M. A., Beau, I., Cole, J. N. S., Dufresne, J. L., … Yokohata, T. (2014). Origins of the solar radiation biases over the Southern Ocean in CFMIP2 models. *Journal of Climate*, *27*, 41–56. https://doi.org/10.1175/JCLI-D-13-00169.1

Bühl, J., Ansmann, A., Seifert, P., Baars, H., & Engelmann, R. (2013). Toward a quantitative characterization of heterogeneous ice formation with lidar/radar: Comparison of CALIPSO/CloudSat with ground-based observations. *Geophysical Research Letters*, *40*, 4404–4408. https://doi.org/10.002/grl.50792

Ceccaldi, M., Delanöe, J., Hogan, R. J., Pounder, N. L., Protat, A., & Pelon, J. (2013). From CloudSat-CALIPSO to EarthCare: Evolution of the DARDAR cloud classification and its comparison to airborne radar-lidar observations. *Journal of Geophysical Research: Atmospheres*, *118*, 7962–7981. https://doi.org/10.1002/jgrd.50579

Ceppi, P., Hartmann, D., & Webb, M. J. (2016). Mechanisms of the negative shortwave cloud feedback in middle to high latitudes. *Journal of Climate*, *29*, 139–157. https://doi.org/10.1175/JCLI-D-15-0327.1

Ceppi, P., Hwang, Y. T., Frierson, D. M. W., & Hartmann, D. L. (2012). Southern Hemisphere jet latitude biases in CMIP5 models linked to shortwave cloud forcing. *Journal of Climate*, *39*, L19708. https://doi.org/10.1029/2012GL053115

Ceppi, P., McCoy, D. T., & Hartmann, D. L. (2016). Observational evidence for a negative shortwave cloud feedback in middle to high latitude. *Geophysical Research Letters*, *43*, 1331–1339. https://doi.org/10.1002/2015GL067499

Ceppi, P., Zelinka, M. D., & Hartmann, D. L. (2014). The response of the Southern Hemispheric eddy-driven jet to future changes in shortwave radiation in CMIP5. *Geophysical Research Letters*, *41*, 3244–3250. https://doi.org/10.1002/2014GL060043

Choi, Y. S., Ho, C. H., Park, C. E., Storelvmo, T., & Tan, I. (2014). Influence of cloud phase composition on climate feedbacks. *Journal of Geophysical Research: Atmospheres*, *119*, 3687–3700. https://doi.org/10.1002/2013JD020582

Chubb, T. H., Jensen, J. B., Siems, S. T., & Manton, M. J. (2013). In situ observations of supercooled liquid clouds over the Southern Ocean during the HIAPER Pole-to-Pole Observation (HIPPO) campaigns. *Geophysical Research Letters*, *40*, 5280–5285. https://doi.org/10.1002/grl.50986

Dee, D. P., Uppala, S. M., Simmons, A. J., Berrisford, P., Poli, P., Kobayashi, S., … Vitart, F. (2011). The ERA-Interim reanalysis: Configuration and performance of the data assimilation system. *Quarterly Journal of the Royal Meteorological Society*, *137*, 553–597. https://doi.org/10.1002/qj.828

Delanöe, J., & Hogan, R. J. (2010). Combined CloudSat-CALIPSO-MODIS retrievals of the properties of ice clouds. *Journal of Geophysical Research*, *115*, D00H29. https://doi.org/10.1029/2009JD012346

Fletcher, J., Mason, S., & Jakob, C. (2016). The climatology, meteorology, and boundary layer structure of marine cold air outbreaks in both hemispheres. *Journal of Climate*, *29*, 1999–2014. https://doi.org/10.1175/jcli-d-15-0268.1

Grise, K. M., Polvani, L. M., & Fasullo, J. T. (2015). Reexamining the relationship between climate sensitivity and the Southern Hemisphere radiation budget in CMIP models. *Journal of Climate*, *28*, 9298–9312. https://doi.org/10.1175/JCLI-D-15-0031.1

Haynes, J. M., Jakob, C., Rossow, W. B., Tselioudis, G., & Brown, J. (2011). Major characteristics of Southern Ocean cloud regimes and their effects on the energy budget. *Journal of Climate*, *24*, 5061–5080. https://doi.org/10.1175/2011jcli4052.1

Hu, Y., Rodier, S., Xu, K., Sun, W., Huang, J., Lin, B., … Josset, D. (2010). Occurrence, liquid water content and fraction of supercooled water clouds from combined CALIOP/IIR/MODIS measurements. *Journal of Geophysical Research*, *115*, D00H34. https://doi.org/10.1029/2009JD012384

Hu, Y., Winker, D., Vaughan, M., Lin, B., Omar, A., Trepte, C., … Holz, R. (2009). CALIPSO/CALIOP cloud phase discrimination algorithm. *Journal of Atmospheric and Oceanic Technology*, *26*, 2293–2309. https://doi.org/10.1175/2009JTECHA1280.1

Huang, Y., Franklin, C. N., Siems, S. T., Manton, M. J., Chubb, T., Lock, A., … Klekociuk, A. R. (2015). Evaluation of boundary-layer cloud forecasts over the Southern Ocean in a limited-area numerical weather prediction system using in-situ, space-borne and ground-based observations. *Quarterly Journal of the Royal Meteorological Society*, *141*, 2259–2276. https://doi.org/10.1002/qj.2519

Huang, Y., Siems, S. T., Manton, M. J., & Thompson, G. (2014). An evaluation of WRF simulations of clouds over the Southern Ocean with A-Train observations. *Monthly Weather Review*, *142*, 647–667. https://doi.org/10.1175/MWR-D-13-00128.1

Huang, Y., Siems, S. T., Manton, M. J., Protat, A., & Delanoë, J. (2012). A study on the low-altitude clouds over the Southern Ocean using the DARDAR-MASK. *Journal of Geophysical Research*, *117*, D18204. https://doi.org/10.1029/2012JD017800

Illingworth, A. J., Hogan, R. J., O'Connor, E. J., Bouniol, D., Delanoë, J., Pelon, J., … Willén, U. (2007). CLOUDNET: Continuous evaluation of cloud profiles in seven operational models using ground-based observations. *Bulletin of the American Meteorological Society*, *88*, 883–898. https://doi.org/10.1175/BAMS-88-6-883

Intrieri, J. M., Shupe, M. D., Uttal, T., & McCarty, B. J. (2002). An annual cycle of Arctic cloud characteristics observed by radar and lidar at SHEBA. *Journal of Geophysical Research*, *107*, 8030. https://doi.org/10.1029/2000JC000423

Kanitz, T., Seifert, P., Ansmann, A., Engelmann, R., Althausen, D., Casiccia, C., & Rohwer, E. G. (2011). Contrasting the impact of aerosols at northern and southern midlatitudes on heterogeneous ice formation. *Geophysical Research Letters*, *38*, L17802. https://doi.org/10.1029/2011GL048532

Kennedy, A., Dong, X., & Xi, B. (2014). Cloud Fraction at the ARM SGP site. Instrument and sampling considerations from 14 years of ARSC. *Theoretical and Applied Climatology*, *115*, 91–105. https://doi.org/10.1007/s00704-013-0853-9

Komurcu, M., Storelvmo, T., Tan, I., Lohmann, U., Yun, Y., Penner, J. E., … Takemura, T. (2014). Intercomparison of the cloud water phase among global climate models. *Journal of Geophysical Research: Atmospheres*, *119*, 3372–3400. https://doi.org/10.1002/2013jd021119

Mace, G. G. (2010). Cloud properties and radiative forcing over the maritime storm tracks for the Southern Ocean and North Atlantic derived from A-Train. *Journal of Geophysical Research*, *115*, D10201. https://doi.org/10.1029/2009JD012517

Marchand, R., Ackerman, T., Smyth, M., & Rossow, W. B. (2009). A review of cloud top height and optical depth histograms from MISR, ISCCP, and MODIS. *Journal of Geophysical Research*, *115*, D16206. https://doi.org/10.1029/2009JD013422

Marchand, R., Ackerman, T., Smyth, M., & Rossow, W. B. (2010). A review of cloud top height and optical depth histograms from MISR, ISCCP, and MODIS. *Journal of Geophysical Research*, *115*, D16206. https://doi.org/10.1029/2009JD013422

McCoy, D. T., Hartmann, D. L., & Grosvenor, D. P. (2014). Observed Southern Ocean cloud properties and shortwave reflection. Part I: Calculation of SW flux from observed cloud properties. *Journal of Climate*, *27*, 8836–8857. https://doi.org/0.1175/JCLI-D-14-00287.1

McCoy, D. T., Hartmann, D. L., Zelinka, M. D., Ceppi, P., & Grosvenor, D. P. (2015). Mixed-phase cloud physics and Southern Ocean cloud feedback in climate models. *Journal of Geophysical Research: Atmospheres*, *120*, 9539–9554. https://doi.org/10.1002/2015JD023603

McCoy, D. T., Tan, I., Hartmann, D. L., Zelinka, M. D., & Storelvmo, T. (2016). On the relationships among cloud cover, mixed-phase partitioning, and planetary albedo in GCMs. *Journal of Advances in Modeling Earth Systems*, *8*, 650–668. https://doi.org/10.1002/2015MS000589

Mioche, G., Jourdan, O., Ceccaldi, M., & Delanoë, J. (2015). Variability of mixed-phase clouds in the Arctic with a focus on the Svalbard region: A study based on spaceborne active remote sensing. *Atmospheric Chemistry and Physics*, *15*, 2445–2461. https://doi.org/10.5194/acp-15-2445-2015

Morrison, A. E., Siems, S. T., & Manton, M. J. (2011). A three-year climatology of cloud-top phase over the Southern Ocean and North Pacific. *Journal of Climate*, *24*, 2405–2418. https://doi.org/10.1175/2010JCLI3842.1

Murray, B. J., O'Sullivan, D., Atkinson, J. D., & Webb, M. E. (2012). Ice nucleation by particles immersed in supercooled cloud droplets. *Chemical Society Reviews*, *41*, 6519–6554. https://doi.org/10.1039/c2cs35200a

Naud, C., Booth, J. F., & Del Genio, A. D. (2014). Evaluation of ERA-Interim and MERRA cloudiness in the Southern Oceans. *Journal of Climate*, *27*, 2109–2124. https://doi.org/10.1175/JCLI-D-13-00432.1

Papritz, L., Pfahl, S., Rudeva, I., Simmonds, I., Sodermann, H., & Wernli, H. (2014). The role of extratropical cyclones and fronts for Southern Ocean freshwater fluxes. *Journal of Climate*, *27*, 6205–6224. https://doi.org/10.1175/JCLI-D-13-00409.1

Protat, A., Armstrong, A., Haeffelin, M., Morille, Y., Pelon, J., Delanoë, J., … Bouniol, D. (2006). Impact of conditional sampling and instrumental limitations on the statistics of cloud properties derived from cloud radar and lidar at SIRTA. *Geophysical Research Letters*, *33*, L11805. https://doi.org/10.1029/2005GL025340

Protat, A., Delanoë, J., O'Connor, E. J., & L'Ecuyer, T. S. (2010). The evaluation of CloudSat and CALIPSO ice microphysical products using ground-based cloud radar and lidar observations. *Journal of Atmospheric and Oceanic Technology*, *27*, 793–810. https://doi.org/10.1175/2009JTECHA1397.1

Protat, A., Young, S. A., McFarlane, S. A., L'Ecuyer, T., Mace, G. G., Comstock, J. M., … Delanoë, J. (2014). Reconciling ground-based and space-based estimates of the frequency of occurrence and radiative effect of clouds around Darwin, Australia. *Journal of Applied Meteorology and Climatology*, *53*, 456–478. https://doi.org/10.1175/JAMC-D-13-072.1

Rauber, R. M., & Tokay, A. (1991). An explanation for the existence of supercooled water at the top of cold clouds. *Journal of the Atmospheric Sciences*, *48*, 1005–1023.

Rossow, W. B., & Schiffer, R. A. (1999). Advances in understanding clouds from ISCCP. *Bulletin of the American Meteorological Society*, *80*, 2261–2287.

Schiffer, R. A., & Rossow, W. B. (1983). The International Satellite Cloud Climatology Project (ISCCP): The first project of the World Climate Research programme. *Bulletin of the American Meteorological Society*, *64*, 779–784.

Seifert, P., Ansmann, A., Mattis, I., Wandinger, U., Tesche, M., Engelmann, R., … Haustein, K. (2010). Saharan dust and heterogeneous ice formation: Eleven years of cloud observations at a central European EARLINET site. *Journal of Geophysical Research*, *115*, D20201. https://doi.org/10.1029/2009JD013222

Shupe, M. D. (2007). A ground-based multisensor cloud phase classifier. *Geophysical Research Letters*, *34*, L22809. https://doi.org/10.1029/2007GL031008

Simmonds, I., Keay, K., & Bye, J. A. T. (2012). Identification and climatology of Southern Hemisphere mobile fronts in a modern reanalysis. *Journal of Climate*, *25*, 1945–1962. https://doi.org/10.1175/JCLI-D-11-00100.1

Stephens, G. L., Vane, D. G., Boain, R. J., Mace, G. G., Sassen, K., Wang, Z., … CloudSat Science Team (2002). A new dimension of space-based observations of clouds and precipitation. *Bulletin of the American Meteorological Society*, *83*, 1771–1790. https://doi.org/10.1175/BAMS-83-12-1771

Storelvmo, T., Tan, I., & Korolev, A. (2015). Cloud phase changes induced by CO_2 warming—A powerful yet poorly constrained cloud-climate feedback. *Current Climate Change Reports*, *1*, 1–9. https://doi.org/10.1007/s40641-015-0026-2

Stubenrauch, C. J., Rossow, W. B., Kinne, S., Ackerman, S., Cesana, G., Chepfer, H., … Zhao, G. (2013). Assessment of global cloud datasets from satellites. *Bulletin of the American Meteorological Society*, *94*, 1031–1049. https://doi.org/10.1175/BAMS-D-12-00117.1

Tan, I., & Storelvmo, T. (2016). Sensitivity study on the influence of cloud microphysical parameters on mixed-phase cloud thermodynamic phase partitioning in CAM5. *Journal of Atmospheric Science*, *73*, 709–728. https://doi.org/10.1175/JAS-D-15-0152.1

Tan, I., Storelvmo, T., & Choi, Y. S. (2014). Spaceborne lidar observations of the ice-nucleating potential of dust, polluted dust, and smoke aerosols in mixed-phase clouds. *Journal of Geophysical Research: Atmospheres*, *119*, 6653–6665. https://doi.org/10.1002/2013JD021333

Tan, I., Storelvmo, T., & Zelinka, M. D. (2016). Observational constraints on mixed-phase clouds imply higher climate sensitivity. *Science*, *352*, 224–227. https://doi.org/10.1126/science.aad5300

Trenberth, K. E., & Fasullo, J. T. (2010). Simulation of present day and 21st century energy budgets of the Southern Oceans. *Journal of Climate*, *23*, 440–454.

Tsushima, Y., Emori, S., Ogura, T., Kimoto, M., Webb, M. J., Williams, K. D., … Andronova, N. (2006). Importance of the mixed-phase cloud distribution in the control climate for assessing the response of clouds to carbon dioxide increase. *Climate Dynamics*, *27*, 113–126. https://doi.org/10.1007/s00382-006-0127-7

Wang, Z., & Sassen, K. (2001). Cloud type and macrophysical property retrieval using multiple remote sensors. *Journal of Applied Meteorology and Climatology*, *40*, 1665–1682.

Wilson, T. W., Ladino, L. A., Alpert, P. A., Breckels, M. N., Brooks, I. M., Browse, J., … Murray, B. J. (2015). A marine biogenic source of atmospheric ice-nucleating particles. *Nature*, *525*, 234–238. https://doi.org/10.1007/s00382-006-0127-7

Winker, D. M., Hunt, W. H., & McGill, M. J. (2007). Initial performance assessment of CALIOP. *Geophysical Research Letters*, *34*, L19803. https://doi.org/10.1029/2007GL030135